

# Minimum Compliance Topology Optimization of Shell-Infill Composites for Additive Manufacturing

Jun Wu<sup>a,\*</sup>, Anders Clausen<sup>b</sup>, Ole Sigmund<sup>b</sup>

<sup>a</sup>*Department of Design Engineering, Delft University of Technology, Delft, The Netherlands*

<sup>b</sup>*Department of Mechanical Engineering, Technical University of Denmark, Lyngby, Denmark*

---

## Abstract

Additively manufactured parts are often composed of two sub-structures, a solid shell forming their exterior and a porous infill occupying the interior. To account for this feature this paper presents a novel method for generating simultaneously optimized shell and infill in the context of minimum compliance topology optimization. Our method builds upon two recently developed approaches that extend density-based topology optimization: A coating approach to obtain an optimized shell that is filled uniformly with a prescribed porous base material, and an infill approach which generates optimized, non-uniform infill within a prescribed shell. To evolve the shell and infill concurrently, our formulation assigns two sets of design variables: One set defines the base and the coating, while the other set defines the infill structures. The resulting intermediate density distributions are unified by a material interpolation model into a physical density field, upon which the compliance is minimized. Enhanced by an adapted robust formulation for controlling the minimum length scale of the base, our method generates optimized shell-infill composites suitable for additive manufacturing. We demonstrate the effectiveness of the proposed method on numerical examples, and analyze the influence of different design specifications.

**Keywords:** Topology optimization, additive manufacturing, two-scale structure, infill, coating, composite

---

## 1. Introduction

Topology optimization has been recognized as an important design method for additive manufacturing, as it fully leverages the manufacturing flexibility enabled by the layer-upon-layer additive process. It finds an optimized material distribution in the design space to maximize the structural performance under given boundary conditions and constraints [1]. Early works in topology optimization are summarized in the book [2], and recent developments until 2013 are reviewed in [3, 4].

While topology optimized material distributions mostly represent solid models, engineering practices in additive manufacturing seem to favour porous structures [5, 6]. In fused deposition modeling (FDM), a commonly used additive manufacturing technology, the interior of 3D

---

\*Corresponding author

Email address: j.wu-1@tudelft.nl (Jun Wu)

11 models is often represented by repetitive infill patterns (e.g., triangles and hexagons). The porous  
12 infill is introduced to control the cost associated with material usage and printing time. The shell-  
13 infill composite involves a few parameters, including the shell thickness, infill pattern, and infill  
14 volume percentage. These parameters are specified by designers to roughly balance cost and  
15 mechanical properties. In general a larger shell thickness and a larger infill volume percentage  
16 lead to a stronger print, while consuming more material and prolonging the printing time.

17 Our current research is motivated from two perspectives. First, post-processing topologi-  
18 cally optimized solids into shell-infill composites guarantees no optimality on the final structure,  
19 thereby wasting the efforts of the sophisticated numerical optimization. It is thus of high in-  
20 terest to consider such a shell-infill composite directly in the structural optimization routine,  
21 eliminating the conversion from optimized solids to sub-optimal shell-infill composites. Second,  
22 shell-infill composites can obtain significantly increased stability with respect to buckling [7]  
23 and unpredicted loading conditions [8] at the expense of a minor increase in compliance. Given  
24 the manufacturing flexibility enabled by additive manufacturing, such two-scale structures have  
25 a high potential to be widely employed in industrial metal printing (e.g., using selective laser  
26 melting).

27 Two recent developments (partially) address the optimal design of shell-infill composites by  
28 extending density-based topology optimization known as SIMP (Solid Isotropic Material with  
29 Penalization) [9]. These two extensions are complementary in the sense that they optimize one  
30 component in the composite, i.e., shell or infill, while assuming the other component prescribed.  
31 Specifically, Clausen et al. [10, 11] proposed a method to design coated structures, i.e., a compo-  
32 sition of a solid shell and base material. The base material can be interpreted as a uniform infill,  
33 with a homogenized stiffness smaller than the stiffness of the solid coating material. The coating-  
34 base structure is obtained by introducing a two-step filtering process to separate the base and the  
35 coating from a scalar field of design variables. Conversely, to optimize infill within a prescribed  
36 shell, Wu et al. [8] presented a method to design bone-inspired micro-structures as porous infill.  
37 This is achieved by introducing an upper bound on a local volume measure, in order to regulate  
38 the local material distribution. The idea of local upper bounds is similar to maximum length  
39 scale [12, 13]. The resulting porous infill is dominated by crossing sub-structures, distributed in  
40 the entire space enclosed by the prescribed solid shell, and following principal stress directions.  
41 The optimized infill performs much stiffer under given boundary conditions than the commonly  
42 used, uniformly repetitive infill patterns.

43 This paper moves a step further and presents a complete solution to the optimal design of  
44 shell-infill composites by concurrently evolving the shell interface and the micro-structural in-  
45 fill. In particular, we propose a novel formulation to consider both the coating-base and infill  
46 constraints in density-based topology optimization. Two design fields are utilized to respectively  
47 derive the coating-base distribution and the infill distribution. The intermediate distributions are  
48 unified by a material interpolation scheme into the final physical density field, based on which the  
49 compliance is minimized. Furthermore, the robust formulation [14] is adapted to ensure length  
50 scale in the composite, leading to distinct infills.

51 The design of shell-infill composites is among recent developments addressing geometric  
52 constraints for additive manufacturing. Langelaar [15], Qian [16], and Gaynor and Guest [17]  
53 proposed methods to ensure the property of self-support in optimized structures. Such methods  
54 follow the filtering scheme proposed by Guest et al. [18] and extended in [19, 12, 20] which are  
55 also the basis of our current work. Wu et al. [21] proposed a rhombic pattern as a special self-  
56 support infill, and performed infill optimization by adaptively subdividing the rhombic cells. The  
57 length scale problem relevant to manufacturing technologies in general is thoroughly examined

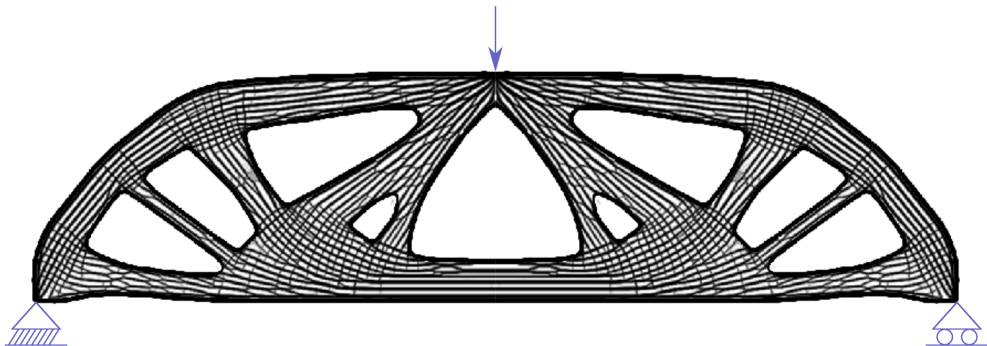


Figure 1: A shell-infill composite obtained from optimizing a simply supported beam.

58 by Lazarov and Wang in [22]. Our method involves and justifies the use of multiple filtering  
 59 steps ( four smoothing steps and three projections in particular ), in addition to the interpolation  
 60 of two design fields and a gradient norm operator. Arguably, it sets a new extreme with respect  
 61 to the number of the involved filtering operations — The most complicated combo of filters  
 62 so far seems to be the four successive filters for the open-close operation suggested in [19].  
 63 Here the four filtering steps and their associated projections are used to control both macro and  
 64 microstructures. Thus beyond proving the new capability of filtering schemes, our method also  
 65 demonstrates the good scalability of multiple filtering in density-based optimization.

66 The remainder of this paper is organized as follows. Section 2 describes the shell-infill com-  
 67 posite our method is aiming at. Section 3 presents the material model of shell-infill composites,  
 68 considering the base, coating, and infill. Section 4 presents the optimization formulation, in-  
 69 cluding local and global volume constraints and sensitivity analysis. Section 5 demonstrates the  
 70 effectiveness of the proposed formulation on numerical examples. Section 6 concludes the paper.

## 71 2. Problem Statement

72 Before we rigorously define the optimization problem in the following sections, let us il-  
 73 lustrate what optimized structures we are aiming at. The composites resulting from numerical  
 74 optimization, without post-processing, shall fulfill a few geometric features. The optimized com-  
 75 posite for a sample beam design problem is shown in Fig. 1. Specifically, the composite structure  
 76 has a shell with a prescribed thickness ( $t$ ), and an infill with a prescribed local volume fraction  
 77 ( $\gamma$ ) at each point in the infill. In the discretized setting, the localized volume fraction of ele-  
 78 ment  $e$  is defined as the number of solid elements over the total number of elements in a small  
 79 neighbourhood around element  $e$ . In this example, the prescribed local volume fraction is 0.6.

80 In the topology optimization process, the shell, including its shape and topology, evolves  
 81 while maintaining the thickness  $t$ . Concurrently evolving is the infill which spreads over the re-  
 82 gion defined by the (dynamically changing) shell. The infill evolves to non-uniformly distributed  
 83 micro-structures, regulated by a constraint on local volume fractions. The concurrent evolution  
 84 of shell-infill is governed by the objective for achieving the highest stiffness under prescribed  
 85 external loads, while respecting a constraint on the global material volume.

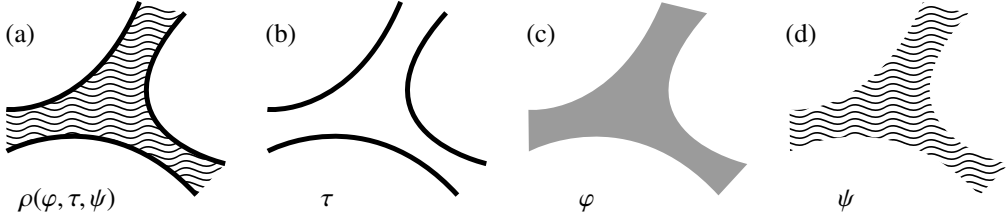


Figure 2: Conceptual illustration of shell-infill composites. The shell-infill structure (a) is composed of a solid shell (b) and a porous infill (d). The shell and infill are related by a base region (c): The shell forms the boundary of the base region, while the infill falls into the base region. A wave infill pattern is used for the illustrative purpose.

### 86 3. Material Model

87 Figure 2 illustrates a conceptual composition of the shell-infill composite (a). It is composed  
 88 of a solid shell (b) and a porous infill (d). These two sub-structures are related by a base region  
 89 (c). The solid shell forms the interface (also called coating in the following) between base region  
 90 and void, and the porous infill spreads across the entire base region. The physical density field  
 91 of the shell-infill composite,  $\rho(\varphi, \tau, \psi)$ , is a function taking as input three intermediate fields, the  
 92 base ( $\varphi$ ), the coating ( $\tau$ ), and the infill ( $\psi$ ).

93 The intermediate density fields are derived from two scalar fields of design variables, defined  
 94 on the design domain  $\Omega$ . From the first field of design variables a two-step filtering process is  
 95 applied to separate the base structure and the coating structure (Section 3.1). From the second  
 96 field of design variables we obtain what can be called an enrichment field, by imposing con-  
 97 straints on a local volume measure (Section 3.2). The integration of intermediate fields into the  
 98 final physical density field is realized by a material interpolation model (Section 3.3).

#### 99 3.1. Coating-Base Structure

100 A two-step filtering process [10] is applied to derive the base and coating structures. As  
 101 illustrated in the left of Fig. 3, the design field,  $\mu$ , is smoothed to get rid of checkerboard patterns,  
 102 giving  $\hat{\mu}$ . The smoothed field is subsequently projected, leading to a sharp base structure,  $\varphi = \tilde{\varphi}$ .  
 103 The smoothing radius ( $R_1$ ) and projection parameters ( $\eta_1$  and  $\beta_1$ ) indirectly control the length  
 104 scale of the base region. The details of the filter implementation are postponed to Section 3.4.

105 To derive the coating layer, a second smoothing (with a filter radius  $R_2$  smaller than  $R_1$ ) is  
 106 applied, giving  $\hat{\varphi}$ . This smoothing is necessary since the base density field  $\varphi$  is non-smooth  
 107 across the sharp edges, and the gradient therefore is not defined. The interface between the base  
 108 region and void is defined by a gradient norm of the smoothed base field  $\hat{\varphi}$ ,

$$||\nabla \hat{\varphi}||_\alpha \equiv \alpha ||\nabla \hat{\varphi}||. \quad (1)$$

109 Here  $||\nabla \hat{\varphi}||$  refers to the Euclidean norm of the spatial gradient of  $\hat{\varphi}$ .  $\alpha$  is a normalization factor  
 110 defined as the inverse of the maximum possible gradient norm of the field  $\hat{\varphi}$ . It can be analytically  
 111 determined that  $\alpha$  relates to  $R_2$  as

$$\alpha = \frac{R_2}{\sqrt{3}}. \quad (2)$$

112 The shell thickness,  $t$ , of the projected sharp coating,  $\tau$ , is prescribed through the smoothing  
 113 radius  $R_2$ :

$$R_2 = \frac{\sqrt{3}}{\ln(2)} t \approx 2.5 t. \quad (3)$$

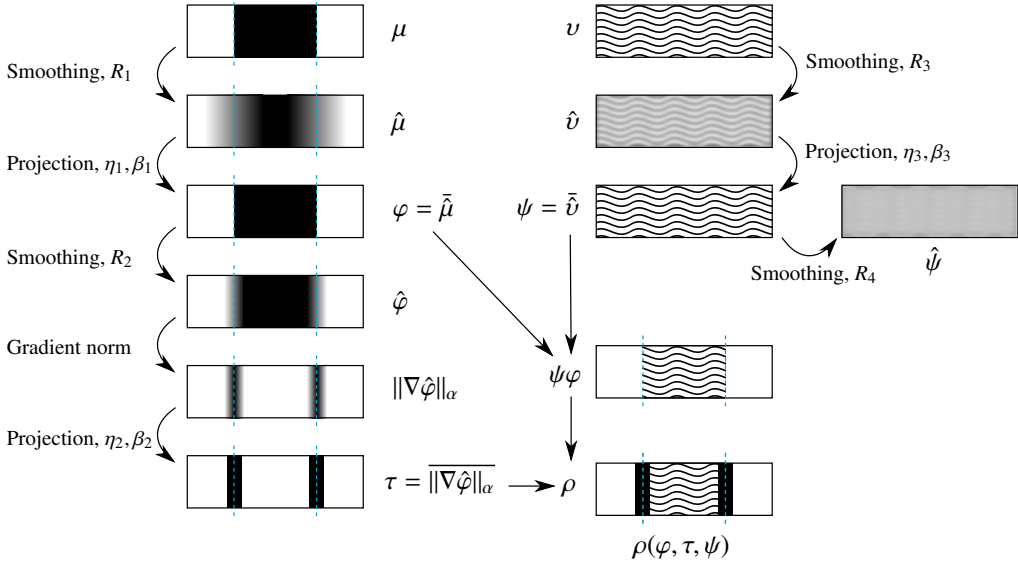


Figure 3: Left, top-down: The first design variable  $\mu$  allows to identify the base region  $\varphi$  and the coating  $\tau$ . The dashed lines indicate the interface as a visual reference. Top right: The second design variable  $v$  defines the infill field  $\psi$ , and the local material measure  $\hat{\psi}$ . A wave infill pattern is used for the illustrative purpose. The actual infill field evolves under constraints imposed on  $\hat{\psi}$ . Bottom right: The intermediate field  $\varphi$ ,  $\tau$ , and  $\psi$  are interpolated to obtain the final physical density field  $\rho$ .

114 Analytical derivations are omitted here but the details can be found in [10].

115 *3.2. Enrichment Field and Local Volume Measure*

116 Rather than prescribing a fixed infill pattern which limits design flexibility [10], the infill  
 117 evolves from a second design field and is decided by the numerical optimization process. The  
 118 enrichment field, as we call the infill field, will be superimposed on the plain base region to create  
 119 fine structures.

120 As illustrated in the top right of Fig. 3, the second design field,  $v$ , is smoothed (giving  $\hat{v}$ ) and  
 121 projected, resulting in a sharp infill field,  $\psi = \bar{\psi}$ . Similar to the first design field, the smoothing  
 122 is to get rid of checkerboard patterns. The smoothing radius ( $R_3$ ) and projection parameters ( $\eta_3$   
 123 and  $\beta_3$ ) indirectly control the length scale, this time, of the infill details.

124 Upon the infill field ( $\psi$ ), a further smoothing is applied, giving  $\hat{\psi}$ . This smoothing is meant to  
 125 quantify the local material accumulation. By imposing an upper bound on this measure, material  
 126 is prevented from forming large solid regions, which thus effectively leads to a porous distribution  
 127 [8]. The constraint will be explained in Section 4.1. For  $\hat{\psi}_e = 1$  (resp.  $\hat{\psi}_e = 0$ ) it means that  
 128 all the elements located in the filtering region  $\mathbb{N}_e$  are black (resp. white). The filtering region for  
 129 element  $e$  is defined as

$$\mathbb{N}_e = \{i \mid \|x_i - x_e\|_2 \leq R_4\}. \quad (4)$$

130 A value of  $\hat{\psi}_e$  between 0 and 1 means that some elements in  $\mathbb{N}_e$  are black and some others  
 131 are white, yet it does not specify which particular elements are black (or white). This allows  
 132 flexibility for the infill evolving to increase the structural stiffness.

133    3.3. Material Interpolation

134    3.3.1. Density Interpolation

135    After getting the intermediate density fields ( $\varphi$ ,  $\tau$ , and  $\psi$ ), the physical density  $\rho$  is defined as  
136    an interpolation:

$$\rho(\varphi, \tau, \psi) = m^0 [\psi\varphi + (1 - \psi\varphi)\tau], \quad (5)$$

137    where  $m^0$  is the mass density of the base material. For simplicity let us assume  $m^0 = 1$  as in the  
138    standard SIMP. The interpolated density  $\rho$  has values in the interval  $[0, 1]$ , since  $\varphi$ ,  $\tau$ , and  $\psi$  obey  
139    the same bound. Considering  $\psi\varphi$  as an integral part, the interpolation of the three fields can be  
140    interpreted as an interpolation of  $\psi\varphi$  and  $\tau$ . This type of interpolation has been studied in [23].

141    We examine this interpolation by considering three extreme cases where the base and coating  
142    fields converge to a discrete 0/1 solution.

- 143    • In the sharp interface defined by  $\tau = 1$  in the coating field, the density interpolation (Eq. 5)  
144    reduces to

$$\rho(\varphi, 1, \psi) = \psi\varphi + (1 - \psi\varphi) \cdot 1 = 1. \quad (6)$$

- 145    • In the base region enclosed by the sharp interface, i.e., defined by  $\varphi = 1$  and  $\tau = 0$ , the  
146    density interpolation reduces to

$$\rho(1, 0, \psi) = \psi \cdot 1 + (1 - \psi \cdot 1) \cdot 0 = \psi. \quad (7)$$

147    In other words, in the base region the enrichment infill field  $\psi$  will be the output.

- 148    • In the void region outside the sharp interface, i.e., defined by  $\varphi = 0$  and  $\tau = 0$ , the density  
149    interpolation reduces to

$$\rho(0, 0, \psi) = \psi \cdot 0 + (1 - \psi \cdot 0) \cdot 0 = 0. \quad (8)$$

150    3.3.2. Stiffness Interpolation

151    In line with the density interpolation from three density fields, the stiffness is interpolated  
152    from three stiffness fields, each of which resembles the standard SIMP stiffness for one density  
153    field,

$$E(\varphi, \tau, \psi) = E^0 [\psi^p \varphi^p + (1 - \psi^p \varphi^p) \tau^p], \quad (9)$$

154    where  $E^0$  is the stiffness of the base material. The penalization parameter  $p = 3$  is the same for  
155    the three fields. The composite stiffness interpolation differs from the standard SIMP interpolation  
156    where the stiffness is defined as an explicit function of the physical density  $\rho$ .

For the three extreme cases (the coating, the base, and the void regions) the stiffness function  
reduces, respectively, to

$$E(\varphi, 1, \psi) = E^0, \quad (10)$$

$$E(1, 0, \psi) = \psi^p E^0, \quad (11)$$

$$E(0, 0, \psi) = 0. \quad (12)$$

157    3.3.3. Two-Material Formulation

The above interpolations assume that the infill and shell have the same material with a mass density of  $m^0 = 1$  and a stiffness of  $E^0$ . To allow the possibility of using a different material for the infill, a scaling factor  $\lambda_m$  for mass density and a factor  $\lambda_E$  for stiffness are applied to the infill field. The interpolations become

$$\rho(\varphi, \tau, \psi) = \lambda_m \psi \varphi + (1 - \lambda_m \psi \varphi) \tau, \quad (13)$$

$$E(\varphi, \tau, \psi) = E^0 [\lambda_E \psi^p \varphi^p + (1 - \lambda_E \psi^p \varphi^p) \tau^p]. \quad (14)$$

158    The scaling factors  $\lambda_m$  and  $\lambda_E$  are contained in the interval  $[0, 1]$ , meaning that the infill  
159    is (optionally) made of a lighter, and softer material than the shell material. We use this two-  
160    material formulation in optimization due to its generality.

161    This two-material formulation reduces to simpler forms in extreme cases. In case of  $\lambda_m = 1$   
162    and  $\lambda_E = 1$ , the two materials have identical mass and stiffness properties, i.e., reducing to the  
163    formulation of a single material. In case of  $\psi = 1$ , i.e., prescribing a fully solid infill field, the  
164    two-material formulation reduces to the standard coating approach [10].

165    3.4. Filters

166    Two types of filters are commonly used in density-based topology optimization. A smoothing  
167    filter applies a convolution operator to smooth the density field. A projection filter thresholds grey  
168    scale values between 0 and 1 into white-or-black values, i.e., either 0 or 1.

169    3.4.1. Smoothing

170    Smoothing filters are applied four times for different purposes. The smoothing of  $\mu \rightarrow \hat{\mu}$  and  
171     $\nu \rightarrow \hat{\nu}$  gets rid of checkerboard patterns (i.e., regions of alternating black and white elements)  
172    resulting from numerical instabilities [24]. The smoothing of  $\varphi \rightarrow \hat{\varphi}$  is to identify the interface  
173    of the base structure. The smoothing of  $\psi \rightarrow \hat{\psi}$  is to quantify the local material accumulation.

174    We use the so-called PDE-filter based on a Helmholtz-type partial differential equation [25].  
175    The PDE-filter is efficient for handling large filter radii. Hence, it is beneficial in the current  
176    work, since the length scale of the base structure necessitates a large filter radius, e.g.,  $R_1 = 24$  in  
177    some of test cases. The smoothed density field is implicitly defined as a solution to the Helmholtz  
178    PDE:

$$-r^2 \nabla^2 \hat{x} + \hat{x} = x, \quad x \in \{\mu, \varphi, \nu, \psi\}. \quad (15)$$

179    The scalar-valued  $r$  is a length scale parameter. Its value is determined by the filter radius,  $R$ , in  
180    the standard filtering technique by a convolution operator,

$$r = \frac{R}{2\sqrt{3}}. \quad (16)$$

181    The filter radius  $R$  indirectly controls the length scale of the respective field. The four radii in the  
182    four smoothing steps generally have different values.

183    The PDE-filter in  $\psi \rightarrow \hat{\psi}$  serves the same purpose as the convolution filter in the original  
184    infill approach [8]: to quantify the local material accumulation. They differ slightly on the  
185    weighting factors: The convolution filter in the original infill approach has a constant weight-  
186    ing factor, while the PDE-filter has a weighting factor gradually decreasing along the outwards  
187    radial direction. We consistently use the PDE-filter for the four smoothing steps in our current  
188    implementation.

189    3.4.2. *Projection*

190    Smoothing operators create density values between 0 and 1. Such grey values are thresholded  
 191    to obtain black-and-white designs by projection methods [18, 19]. Differentiable projections are  
 192    used to facilitate gradient-based numerical optimization. We use the projection function proposed  
 193    in [14]:

$$\bar{x}_i = \frac{\tanh(\beta\eta) + \tanh(\beta(x_i - \eta))}{\tanh(\beta\eta) + \tanh(\beta(1 - \eta))}, \quad x \in \{\hat{\mu}, \|\nabla\hat{\varphi}\|_\alpha, \hat{v}\}. \quad (17)$$

194    m The projection is parametrized by two values, the ‘sharpness’ value,  $\beta$ , and the threshold value,  
 195     $\eta \in [0, 1]$ . The differentiable function approaches a discontinuous step function in the limit of  
 196     $\beta \rightarrow \infty$ . A parameter continuation process starting from a small  $\beta$  value is applied to improve  
 197    convergence behaviour, in contrast to directly starting with a very large  $\beta$  value.

198    Denote the projected field for  $\eta = 0.5$  as a reference field. A larger threshold value of  $\eta > 0.5$   
 199    results in an eroded field compared to the reference field. As  $\eta$  approaches 1 the projection  
 200    becomes similar to the modified Heaviside step function [19]. A smaller threshold value of  
 201     $\eta < 0.5$  results in a dilated field compared to the reference field. As  $\eta$  approaches 0 the projection  
 202    becomes similar to the Heaviside step function [18].

203    In the three projection steps resulting in the physical density field, we choose the same thresh-  
 204    old value of  $\eta_{1,2,3} = 0.5$ . We note that an eroded projection by  $\eta > 0.5$  can be applied to control  
 205    the length scale. This will be discussed in Section 4.3 where we explore this possibility to control  
 206    the length scale of the base structure.

207    4. Shell-Infill Optimization

We consider a standard compliance minimization problem. However, besides a constraint on the global volume as in standard topology optimization, a constraint is imposed on the local volume measure obtained from the second design field. The optimization problem is defined as follows.

$$\min_{\mu, \nu} \quad c = \mathbf{U}^T \mathbf{K} \mathbf{U}, \quad (18)$$

$$\text{s.t.} \quad \mathbf{K} \mathbf{U} = \mathbf{F}, \quad (19)$$

$$l(\boldsymbol{\nu}) \leq 0, \quad (20)$$

$$g(\boldsymbol{\mu}, \boldsymbol{\nu}) \leq 0, \quad (21)$$

$$\mu_e, \nu_e \in [0, 1], \quad \forall e. \quad (22)$$

208    Here  $c$  is the compliance.  $\mathbf{U}$ ,  $\mathbf{K}$ , and  $\mathbf{F}$  are displacement vector, stiffness matrix, and force vector,  
 209    respectively. The functions  $l$  and  $g$  represent local and global volume constraint, respectively.  $\boldsymbol{\mu}$   
 210    and  $\boldsymbol{\nu}$  are vectors of element values in the design fields  $\mu$  and  $\nu$ , respectively. The subscript  
 211     $e$  indicates an element in the design domain. The global stiffness matrix  $\mathbf{K}$  is assembled from  
 212    element stiffness matrix  $\mathbf{k}_e$ , which is defined as:

$$\mathbf{k}_e = E_e(\varphi_e, \tau_e, \psi_e) \mathbf{k}_0, \quad (23)$$

213    where  $\mathbf{k}_0$  is the element stiffness matrix for an element with unit Young’s modulus. To prevent  
 214    the global stiffness matrix from becoming singular, a small minimum stiffness  $\lambda_{E,\min} E^0$  is used  
 215    to represent void element. This modifies the term  $\lambda_E \psi^P \varphi^P$  in Eq. 14 to  $\lambda_{E,\min} + (\lambda_E - \lambda_{E,\min}) \psi^P \varphi^P$ .

216 In the following we discuss the local volume constraint (Section 4.1), the global volume  
 217 constraint (Section 4.2), the application of a length scale (Section 4.3), and the sensitivity analysis  
 218 (Section 4.4). The optimization problem is solved based on sensitivities using the method of  
 219 moving asymptotes (MMA) [26].

220 *4.1. Local Volume Constraints (Infill)*

221 Local volume constraints regulate the local (infill) material distribution. For each element in  
 222 the second design field, a constraint is imposed,

$$\hat{\psi}_e \leq \gamma, \forall e \quad (24)$$

223 with  $\gamma$  being the upper bound on the local volume fraction. The upper bound is a fixed parameter  
 224 specified by the designer. For a prescribed value smaller than 1, the local volume constraint  
 225 prevents material from forming large solid parts. For instance,  $\gamma = 0.5$  leads to a material  
 226 distribution where, in the neighbourhood of each element, at most 50% elements can become  
 227 solid. The neighbourhood is defined by the filter radius  $R_4$ . This upper bound thus controls the  
 228 local porosity.

229 The number of local volume constraints equals the number of elements. To facilitate efficient  
 230 numerical optimization, we use the  $p$ -norm to approximate the maximum value in  $\hat{\psi}$ ,

$$\|\hat{\psi}\|_{p_n} = \left( \sum_e \hat{\psi}_e^{p_n} \right)^{1/p_n} \approx \max_{\forall e} (\hat{\psi}_e). \quad (25)$$

231 Here  $p_n$  denotes the  $p$ -norm parameter, to distinguish from the penalization  $p$ . This approxima-  
 232 tion reduces constraints Eq. 24 to a single, differentiable constraint,

$$\|\hat{\psi}\|_{p_n} \leq \gamma. \quad (26)$$

233 As  $p_n$  goes to infinity, the approximation error between the  $p$ -norm and max function becomes  
 234 zero. To account for the approximation error when the value of  $p_n$  is not infinitely large, we  
 235 modify the aggregated constraint to

$$\left( \sum_e \hat{\psi}_e^{p_n} \right)^{1/p_n} \leq \left( \sum_e \gamma^{p_n} \right)^{1/p_n}, \quad (27)$$

236 yielding the local volume constraint,

$$l(\mathbf{v}) = \left( \frac{1}{n} \sum_e \hat{\psi}_e^{p_n} \right)^{1/p_n} - \gamma \leq 0, \quad (28)$$

237 where  $n$  is the number of elements.

238 *4.2. Global Volume Constraint*

239 The global volume is accumulated from the physical density field  $\rho$ . A straightforward global  
 240 volume constraint takes the form

$$\sum_{\forall e} \rho_e v_e \leq V^*, \quad (29)$$

241 where  $v_e$  is the (constant) element volume, and  $V^*$  is the maximum allowed volume.



Figure 4: Left: The shell-infill composite obtained with the global volume constraint Eq. 29. Multiple large void parts appear in the base region, counteracting the intent to have distributed infill. Right: Composite obtained with the updated global volume constraint Eq. 31. Infill spreads over the entire base, making a clearly distinguishable shell-infill composite. The compliance is 98.2 (left) and 108.0 (right).

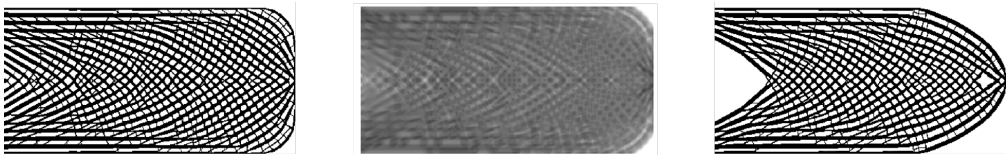


Figure 5: Left: The infill ( $\psi$ ) obtained with an upper bound  $\gamma = 0.6$  as local volume constraints, assuming the entire design space is a prescribed base region. No global volume constraint is imposed. Middle: The field of local volume measure  $\hat{\psi}$ . The local volume measures reach the upper bound  $\gamma$  in the entire base region. Right: When a global volume constraint of ratio 0.5 is imposed, the infill shrinks to satisfy this constraint, leaving large void parts in the base region.

242 However, experimental tests show that when combined with local volume constraints for  
 243 the infill, this global volume formulation leads to unintended structures. See Fig. 4 (left) for  
 244 instance. Inside the base region, there are large void parts. These large voids counteract the  
 245 design intention to have distinct shell-infill structures where the infill spreads over the entire base  
 246 region enclosed by the shell.

247 To explain this, let us consider the simple case where the design space is a prescribed base  
 248 region, i.e., the standard infill approach [8]. When the local volume constraints are imposed  
 249 while the global volume constraint is inactive, the infill will spread over the entire base region  
 250 (see Fig. 5 left): At each element, the local volume measure will reach the prescribed upper bound  
 251 (see Fig. 5 middle for the field  $\hat{\psi}$ ). This is in line with compliance minimization: The optimal  
 252 structure always tries to exploit the full amount of material. If the global volume allowance for  
 253 this region is smaller than necessary to spread the infills, (unintended) large void parts will have  
 254 to be created (see Fig. 5 right).

255 Since the amount of base region in the concurrent optimization is not known *a priori*, the idea  
 256 is that the allowed volume for infill shall be proportional to the area of the base region, rather  
 257 than merely the area occupied by the sparse infill as in Eq. 29. In particular, assuming that every  
 258 element takes the grey value of the upper bound  $\gamma$ , the physical density field becomes

$$\hat{\rho}(\varphi, \gamma, \tau) = \lambda_m \gamma \varphi + (1 - \lambda_m \gamma \varphi) \tau. \quad (30)$$

259 The updated global volume constraint, in its normalized version, is

$$g(\mu, \gamma) = \left( \sum_e \hat{\rho}_e v_e \right) / V^* - 1 \leq 0. \quad (31)$$

260 As can be seen on the right of Fig. 4, the updated global volume constraint serves the purpose  
 261 of having infill spread over the base region. This updated global volume constraint is conserva-

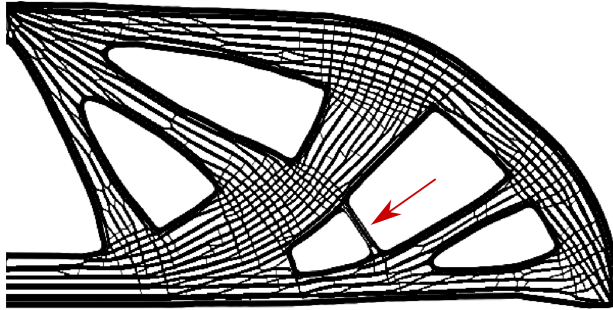


Figure 6: The shell-infill composite degenerates to a partial shell segment enclosing no infill, indicated by the arrow.

262      tive, in the sense that the global volume from the real physical density  $\rho$  is smaller than that from  
263      the approximated density  $\hat{\rho}$ , i.e.,

$$\sum_{\forall e} \rho_e v_e \leq \sum_e \hat{\rho}_e v_e. \quad (32)$$

264      The two volumes become equal when the infill field takes the upper bound  $\gamma$  for every element.  
265      As the infill converges to a discrete 0/1 solution, the left becomes smaller. Consider the simple  
266      case of Fig. 5 where the entire design space is a prescribed base region. An upper local volume  
267      bound  $\gamma = 0.6$  leads to a global volume ratio of 0.53 (Fig. 5 left).

#### 268      4.3. Length Scale

269      Length scale of the base is an additional option to help achieving distinct shell-infill com-  
270      posites. When the width of the base region is small, shell-infill locally degenerates to a shell  
271      enclosing no infill (See Fig. 6 for an example). To prevent this, we adapt the robust formula-  
272      tion [14, 27] to ensure a minimum length scale of the base. The robust formulation applies an  
273      erosion and a dilation projection, along with the intermediate projection. The projection parame-  
274      ter has been explained in Section 3.4.2, Eq. 17. By optimizing the structural performance on the  
275      worst scenario among the three projections, a minimum length scale on the solid and void phase  
276      can be ensured, resulting from the erosion and dilation projection, respectively.

277      In the context of compliance minimization, the worst case (i.e., the highest compliance value)  
278      among the three projections is the density field associated with erosion, since it uses the least  
279      amount of material. In the context of shell-infill optimization, while minimizing this worst case  
280      indeed ensures a length scale of the base, the coating at some locations is not clearly defined. An  
281      example is shown in Fig. 7 (top) for the standard coating approach, i.e., the infill constraint is not  
282      yet imposed for simplicity. The left and right are the coating-base structures corresponding to  
283      the intermediate and erosion projection, respectively. The coating in the intermediate projection  
284      (a) does not contribute in any way to the objective function, since the objective considers only  
285      the erosion projection which has a larger compliance value.

286      To encourage the appearance of a well-defined coating in the intermediate projection, the  
287      idea is to consider both the erosion projection and the intermediate projection in the robust for-  
288      mulation. Specifically, the following objective is minimized,

$$c = \omega \mathbf{U}^T \mathbf{K} \mathbf{U} + (1 - \omega) \mathbf{U}^{eT} \mathbf{K}^e \mathbf{U}^e, \quad (33)$$

289      where  $\omega$  is a weighting factor, and the superscript  $e$  in the second term indicates the eroded  
290      version. Figure 7 (bottom) demonstrates that the coating in the intermediate version is restored.

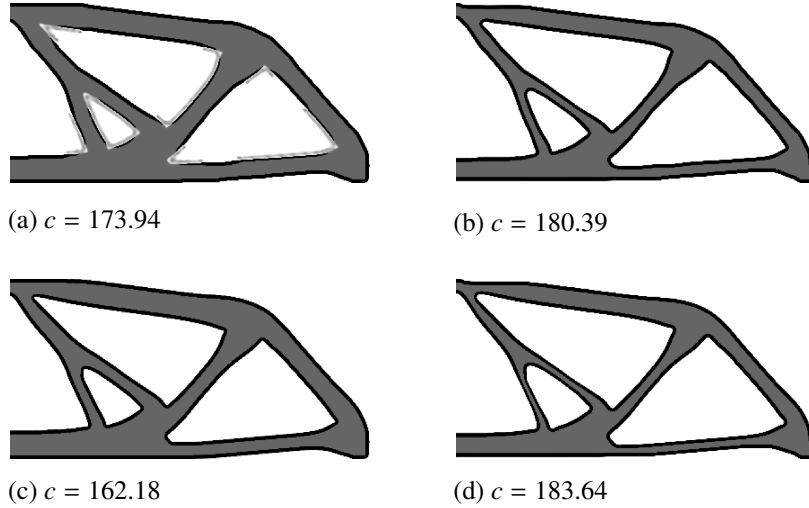


Figure 7: Coating in the intermediate density field (a) is not well defined if only the compliance of the eroded version (b) is minimized in the objective function. Bottom: By minimizing both the intermediate and eroded versions, it encourages the appearance of the coating in the intermediate version (c). Both are tested with  $v = 0.3$ ,  $\gamma = 1$ ,  $\lambda_m = 0.6$ , and  $\lambda_E = 0.33$ .

291 We note that this combined objective function is an approximate approach to ensure length scale,  
 292 since it involves a weighting factor. A small  $\omega$  value leads to a shell which is not well defined,  
 293 while a large  $\omega$  value may lead to a structure violating the length scale. A continuation is applied  
 294 in our test:  $\omega$  is gradually increased from 0.1 to 0.8, by an increment of 0.1 every 50 iterations.

295 **4.4. Sensitivity Analysis**

296 For solving the optimization problem defined by Eqs. 18-22 using the gradient-based MMA  
 297 solver, the following sensitivities are needed:

$$\frac{\partial c}{\partial \mu_e}, \frac{\partial c}{\partial v_e}, \frac{\partial l}{\partial \mu_e}, \frac{\partial l}{\partial v_e}, \frac{\partial g}{\partial \mu_e}, \text{ and } \frac{\partial g}{\partial v_e}. \quad (34)$$

298 All these sensitivities are elaborated in the following paragraphs.

299 (1)  $\partial c / \partial \mu_e$  and  $\partial c / \partial v_e$ . From adjoint analysis the sensitivities of the compliance objective are:

$$\frac{\partial c}{\partial x_e} = -\mathbf{U}^T \frac{\partial \mathbf{K}}{\partial x_e} \mathbf{U} = -\sum_i \frac{\partial E_i}{\partial x_e} (\mathbf{u}_i^T \mathbf{k}^0 \mathbf{u}_i), \quad x \in \{\mu, v\} \quad (35)$$

300 To derive  $\partial E_i / \partial \mu_e$  and  $\partial E_i / \partial v_e$ , we rewrite the stiffness interpolation (Eq. 14) by

$$E(\varphi, \tau, \psi) = E^0 [\lambda_E \psi^p \varphi^p + (1 - \lambda_E \psi^p \varphi^p) \tau^p] = E^0 \left[ \underbrace{\lambda_E \psi^p \varphi^p}_{A_E} + \underbrace{\tau^p}_{B_E} - \underbrace{\lambda_E \psi^p \varphi^p \tau^p}_{C_E} \right]. \quad (36)$$

301 Considering that  $\psi(v)$  is independent of the first design variable  $\mu$ , and applying the chain rule  
 302 and product rule, we arrive at

$$\frac{\partial E_i}{\partial \mu_e} = E^0 \left[ \frac{\partial A_E}{\partial \varphi_i} \frac{\partial \varphi_i}{\partial \mu_e} + \frac{\partial B_E}{\partial \tau_i} \frac{\partial \tau_i}{\partial \mu_e} - \frac{\partial C_E}{\partial (\varphi_i \tau_i)} \left( \tau_i \frac{\partial \varphi_i}{\partial \mu_e} + \varphi_i \frac{\partial \tau_i}{\partial \mu_e} \right) \right], \quad (37)$$

303 with  $\partial A_E / \partial \varphi_i = \lambda_E \psi_i^b b \varphi_i^{b-1}$ ,  $\partial B_E / \partial \tau_i = b \tau_i^{b-1}$ , and  $\partial C_E / \partial (\varphi_i \tau_i) = \lambda_E \psi_i^b b (\varphi_i \tau_i)^{b-1}$ .

304 Similarly, considering  $\varphi(\mu)$  and  $\tau(\mu)$  are independent of  $v$ , this leads to

$$\frac{\partial E_i}{\partial v_e} = E^0 \left[ \frac{\partial A_E}{\partial \varphi_i} \frac{\partial \psi_i}{\partial v_e} - \frac{\partial C_E}{\partial \varphi_i} \frac{\partial \psi_i}{\partial v_e} \right], \quad (38)$$

305 with  $\partial A_E / \partial \psi_i = \lambda_E \varphi_i^p p \psi_i^{p-1}$  and  $\partial C_E / \partial \psi_i = \lambda_E \varphi_i^p \tau_i^p p \psi_i^{p-1}$ .

306 (2)  $\partial l / \partial \mu_e$  and  $\partial l / \partial v_e$ . The sensitivities of the local volume constraint with respect to the design  
307 variables has the form

$$\frac{\partial l}{\partial x_e} = \sum_i \left( \sum_j \left( \frac{\partial l}{\partial \hat{\rho}_j} \frac{\partial \hat{\rho}_j}{\partial \rho_i} \right) \frac{\partial \rho_i}{\partial x_e} \right), \quad x \in \{\mu, v\}, \quad (39)$$

308 with

$$\frac{\partial l}{\partial \hat{\rho}_j} = \frac{1}{n} \left( \frac{1}{n} \sum_e \hat{\rho}_e^{p_n} \right)^{1/p_n-1} \hat{\rho}_j^{p_n-1}. \quad (40)$$

309 To derive  $\partial \rho_i / \partial \mu_e$ , Eq. 13 is rewritten as

$$\rho(\varphi, \tau, \psi) = \lambda_m \psi \varphi + (1 - \lambda_m \psi \varphi) \tau = \underbrace{\lambda_m \psi \varphi}_{A_m} + \underbrace{\tau}_{B_m} - \underbrace{\lambda_m \psi \varphi \tau}_{C_m}. \quad (41)$$

310 Again, considering that  $\psi(v)$  is independent of  $\mu$ , and applying the chain rule and product rule, it  
311 leads to

$$\frac{\partial \rho_i}{\partial \mu_e} = \frac{\partial A_m}{\partial \varphi_i} \frac{\partial \varphi_i}{\partial \mu_e} + \frac{\partial B_m}{\partial \tau_i} \frac{\partial \tau_i}{\partial \mu_e} - \frac{\partial C_m}{\partial (\varphi_i \tau_i)} \left( \tau_i \frac{\partial \varphi_i}{\partial \mu_e} + \varphi_i \frac{\partial \tau_i}{\partial \mu_e} \right), \quad (42)$$

312 with  $\partial A_m / \partial \varphi_i = \lambda_m \psi_i$ ,  $\partial B_m / \partial \tau_i = 1$ , and  $\partial C_m / \partial (\varphi_i \tau_i) = \lambda_m \psi_i$ .

313 For the design variable  $v$ , we have

$$\frac{\partial \rho_i}{\partial v_e} = \frac{\partial A_m}{\partial \psi_i} \frac{\partial \psi_i}{\partial v_e} - \frac{\partial C_m}{\partial \psi_i} \frac{\partial \psi_i}{\partial v_e}, \quad (43)$$

314 with  $\partial A_m / \partial \psi_i = \lambda_m \varphi_i$  and  $\partial C_m / \partial \psi_i = \lambda_m \varphi_i \tau_i$ .

315 (3)  $\partial g / \partial \mu_e$  and  $\partial g / \partial v_e$ . The derivative of the total volume constraint with respect to the design  
316 variables is:

$$\frac{\partial g}{\partial x_e} = \sum_j \hat{\rho}_j \sum_i \frac{\partial \hat{\rho}_i}{\partial x_e}, \quad x \in \{\mu, v\}. \quad (44)$$

317 The modified density  $\hat{\rho}_i$  is independent of  $v$ , leading to

$$\frac{\partial \hat{\rho}_i}{\partial v_e} = 0. \quad (45)$$

318  $\partial \hat{\rho}_i / \partial \mu_e$  is a modified version of Eq. 42 by replacing  $\psi$  therein with  $\gamma$ ,

$$\frac{\partial \hat{\rho}_i}{\partial \mu_e} = \lambda_m \gamma \frac{\partial \varphi_i}{\partial \mu_e} + \frac{\partial \tau_i}{\partial \mu_e} - \lambda_m \gamma \left( \tau_i \frac{\partial \varphi_i}{\partial \mu_e} + \varphi_i \frac{\partial \tau_i}{\partial \mu_e} \right). \quad (46)$$

319 (4) Elementary Derivatives. In above formulations, some elementary derivatives (e.g.,  $\partial \varphi / \partial \mu$ ,  
320  $\partial \tau / \partial \mu$ , and  $\partial \psi / \partial v$ ) are not included here, but can be found in [10, 8].

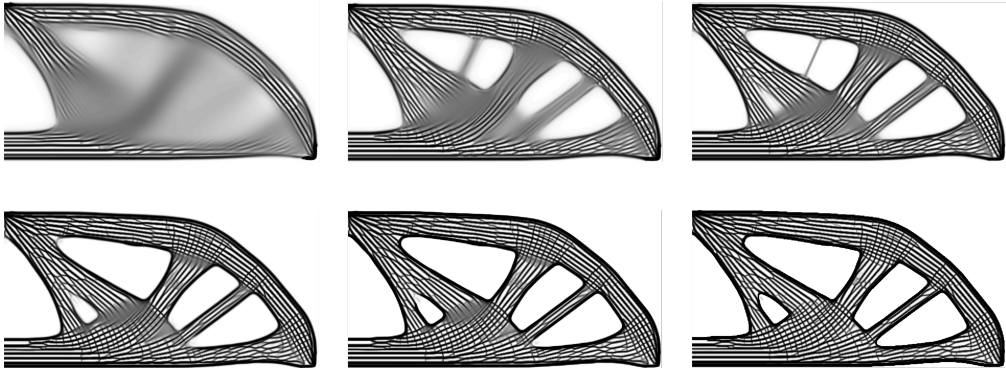


Figure 8: The shell-infill composite during the iterative optimization process. From left to right and top to down, the density distribution at the iterations of 100, 200, 300, 400, 500, 1000.

## 321 5. Results

322 In this section we demonstrate the effectiveness of the proposed topology optimization for  
 323 different examples. Variations of the optimized structures with respect to different design speci-  
 324 fication will be analyzed, to explain the consequence of the involved parameters.

325 The following parameters are the same for all examples. The constraints aggregation is cal-  
 326 culated with a p-norm value of  $p_n = 8$ . A penalization  $p = 3$  is used in the stiffness interpolation  
 327 (Eq. 9) for  $\psi$ ,  $\varphi$ , and  $\tau$ . A projection threshold 0.5 is used for  $\eta_1$ ,  $\eta_2$ , and  $\eta_3$ , while the eroded  
 328 version of the base takes a value of 0.7. Parameter continuation is applied for the sharpness pa-  
 329 rameters. The coating sharpness is initialized with  $\beta_2 = 8$  to get a sharp coating already from the  
 330 beginning of the optimization, and doubled at every 100th iteration (or at convergence) until it  
 331 is increased to 64. The sharpness of base and infill starts from  $\beta_{1,3} = 1$ , and is doubled together  
 332 with  $\beta_2$ .

### 333 5.1. Simply supported beam

334 The first example is a simply supported beam, as shown in Fig. 1. Due to symmetry only one  
 335 half of the design domain is simulated. The half design domain is discretized by square elements  
 336 with a resolution of  $300 \times 600$  to accommodate fine scale infill structures.

337 The problem is optimized using a total volume fraction of 40%, and an upper local volume  
 338 bound of 0.6. The four smoothing filter radii are  $R_1 = 24$  for the base,  $R_2 = 15$  for the coating  
 339 (i.e., leading to a coating thickness of  $t = 6$ ),  $R_3 = 2$  for the infill, and  $R_4 = 8$  for quantifying the  
 340 local volume fraction, all measured in terms of elements. The intermediate domains are extended  
 341 from the design domain by a size of the largest filter radius ( $R_1$ ) in order to ensure the length scale  
 342 on the boundary [28].

343 Figure 8 shows a sequence of the shell-infill composite during the design progression. As the  
 344 optimization progresses, a clear shell-infill structure emerges from the grey density distribution.  
 345 The optimized result shows two scales. The coarser scale defined by the shell looks familiar to  
 346 standard topology optimization. Enclosed by the shell, the infill varies in different subregions,  
 347 following the direction of the internal uni-axial stresses. This can be attributed to the fact that  
 348 on the coarse scale as in standard topology optimization the optimized structure receives highly  
 349 uni-axial stresses (compression or tension). At the joints connecting two bars, there are crossing

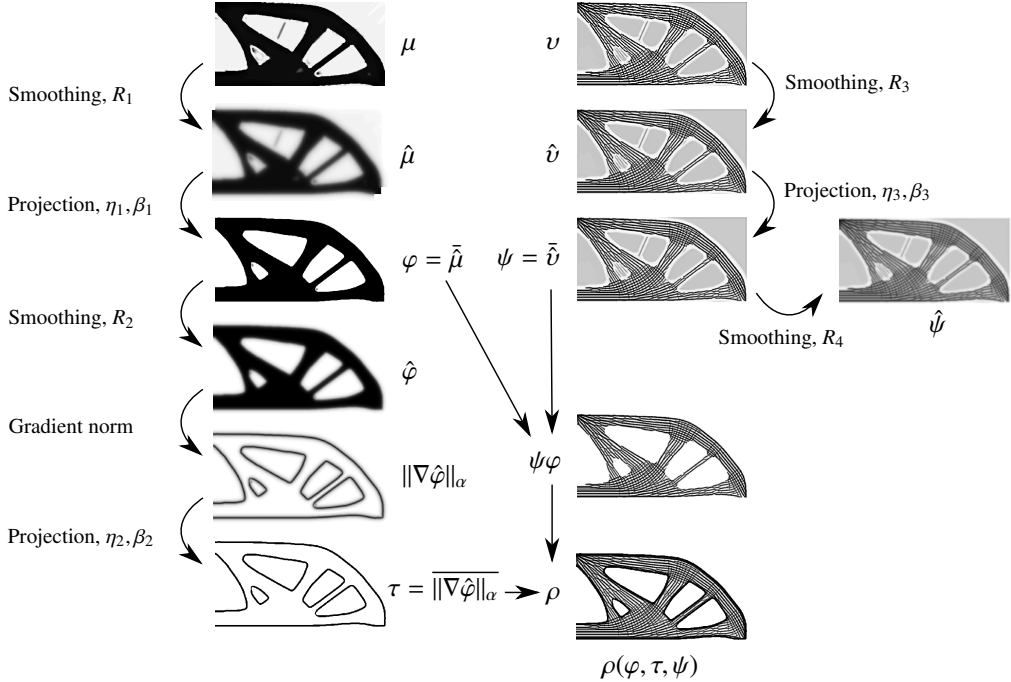


Figure 9: The intermediate density distributions involved in the shell-infill optimization of the sample beam.

350 structures which naturally flow in from the infills in the adjacent branches, indicating bi-axial  
 351 stresses in the crossings.

352 Figure 9 displays the intermediate density distributions involved in the shell-infill compo-  
 353 sition. The layout of this figure follows the schematic illustration in Fig. 3. On the left, from  
 354 top to bottom, the density field of the first design variable is smoothed and projected to obtain a  
 355 black-white base field  $\varphi$ . The base is smoothed, allowing its interface to be extracted by the  
 356 gradient norm. The interface is further projected to obtain a sharp coating layer  $\tau$ . On the right, the  
 357 density field of the second design variable evolves to a porous infill  $\psi$ . Due to the local volume  
 358 constraints, the material forms small scale geometrical details in the region corresponding to the  
 359 (black) base on the left. Since the enrichment field outside the base region does not affect the  
 360 stiffness of the final composite structure, this outside region shows a uniform grey.

### 361 5.2. Cantilever Beam

362 The second numerical test is a cantilever beam. The design domain and boundary conditions  
 363 are illustrated in Fig. 10. Due to symmetry only one half of the design domain is optimized, by  
 364 using a discretization of  $150 \times 500$  square elements. The resulting half structure is completed by  
 365 its mirrored image to illustrate a complete structure.

366 The problem is optimized using a total volume fraction of 36%. Different local volume upper  
 367 bounds ( $0.4 \sim 0.7$ ) are applied to analyze the variations. The four filter radii in these tests are  
 368  $R_1 = 16$ ,  $R_2 = 10$ ,  $R_3 = 2$ , and  $R_4 = 8$ , all measured in terms of elements.

369 Figure 11 shows the four shell-infill composites with different infill porosities. As the local  
 370 volume upper bound increases, the infill becomes denser. Since the same total volume constraint



Figure 10: The design domain and boundary condition of the cantilever beam.

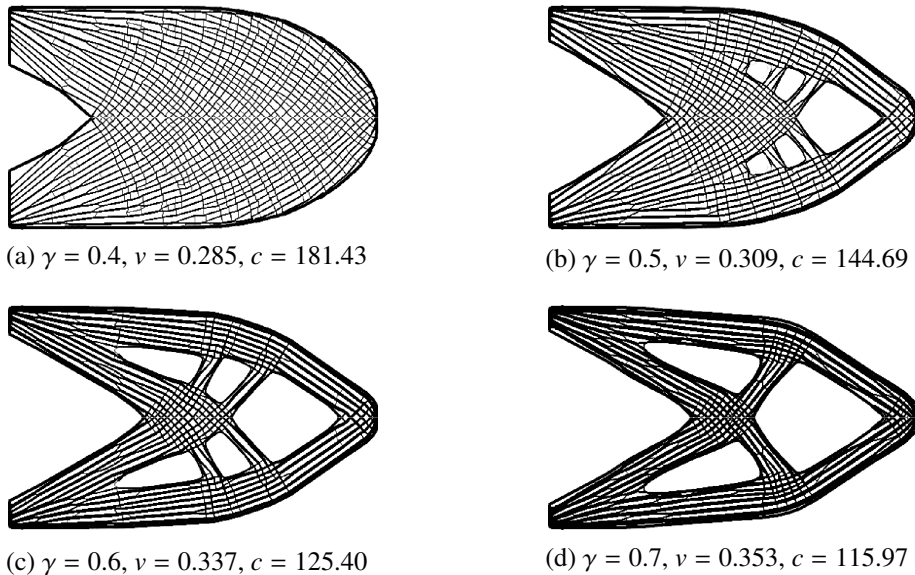


Figure 11: Cantilever beam example with different local volume upper bounds.

371 is applied, the denser infill results in a reduction of the base region. The compliance value also  
 372 reduces as the infill becomes denser. To exclude the influence of the different volume values  
 373 (which result from the infill approximation explained in Section 4.2), the compliance-volume  
 374 ratios ( $c/v$ ) are calculated. In the order of an increasing infill fraction the ratios are 636.6, 468.3,  
 375 372.1, and 328.5, respectively.

### 376 5.3. Multiple Loads

377 Triangular-shaped (macro-)structures perform well for multiple, individually applied loads.  
 378 Also, so-called rank-3 materials are optimal for microstructures subjected to multiple load cases.  
 379 Hence, it is interesting to see whether such triangular-shaped structures also appear in the opti-  
 380 mized infill when considering multiple load cases. Fig. 12 shows the design domain of a simply  
 381 supported beam, upon which five vertical loads are applied individually. The objective function is  
 382 the average of five compliances, each of which corresponds to an individual load. Fig. 13 shows  
 383 the optimized shell-infill in this multi-load case. The multiple loads result in more variations of  
 384 infill pattern than seen in the previous single load case problems. In particular, some triangular

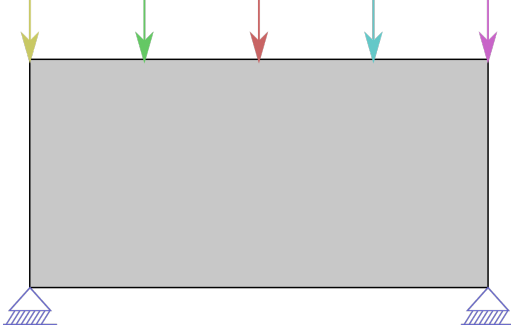


Figure 12: Design domain of a simply supported beam. The five loads have the same magnitude, and are applied individually.

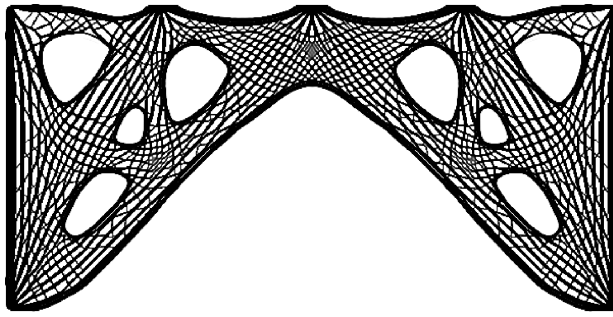


Figure 13: Optimized shell-infill for 5 individually applied loads.

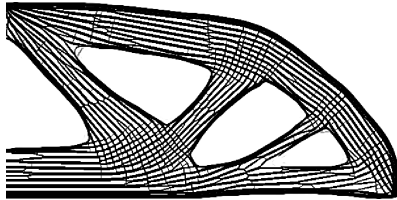
385 sub-structures do appear and other regions have laminations that do not cross at right angles as  
386 was the rule in the single load case structures.

387 The domain has a resolution of  $300 \times 600$  in terms of square finite elements. It is optimized  
388 with a maximum total volume fraction 36%, a local volume upper bound 0.6,  $R_1 = 16$ ,  $R_2 = 10$ ,  
389  $R_3 = 2$ , and  $R_4 = 8$ .

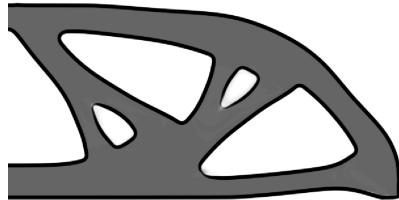
390 *5.4. Comparison of Infills*

391 We compare the present optimization of shell-infill composites against the standard coating  
392 approach. The uniform infill in the standard coating approach can be interpreted as a prescribed,  
393 repetitive infill pattern. We first run the concurrent optimization with a local volume upper bound  
394  $\gamma = 0.6$ , and a total volume constraint of 0.4. The obtained physical density field amounts to a  
395 total volume of 0.368. With this total volume, we run the standard coating approach. Here, we  
396 assume the density of the uniform infill is 0.6, the same value as the local upper bound in the  
397 shell-infill composite. The uniform infill is made of the same material as the coating. According  
398 to the Hashin-Shtrikman bounds for isotropic material [29], a density of 0.6 leads to a maximum  
399 effective stiffness of  $1/3$ . The two structures obtained using these two approaches are shown in  
400 Fig. 14. The numerical analysis suggests that the non-uniform infill performs much stiffer than  
401 the uniform infill for the same material volume.

402 The same conclusion can be drawn from a comparison performed on the cantilever beam  
403 model. The structures are shown in Fig. 15. The shell in these two designs has the same topology,

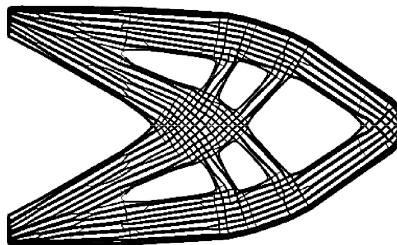


(a)  $\gamma = 0.6, \lambda_m = 1.0, c = 106.92$

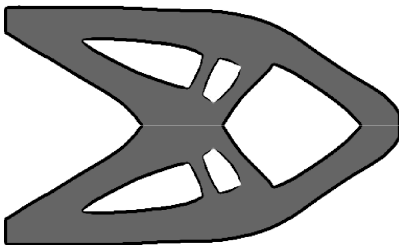


(b)  $\gamma = 1.0, \lambda_m = 0.6, c = 146.08$

Figure 14: Left: The shell-infill composite with an infill varying according to the stress distribution. Right: The infill is uniform. Both design use the same amount of total volume ( $v = 0.368$ ).



(a)  $\gamma = 0.6, \lambda_m = 1.0, c = 125.40$



(b)  $\gamma = 1.0, \lambda_m = 0.6, c = 176.98$

Figure 15: A comparison of the non-uniform infill (left) and uniform infill (right) on the cantilever beam model. Both design use the same amount of total volume ( $v = 0.337$ ).

404 while its contour varies slightly. The uniform infill (right) has a larger compliance value.

405 The improved performance of the optimized infill structures come at the cost of an ex-  
406 pected decreased local buckling stability in the uni-axially loaded compression regions. Here  
407 single scale laminates will have low buckling stability but this may potentially be avoided by an  
408 anisotropic filtering approach suggested for the same reasons in our previous work [8].

#### 409 5.5. Two Materials

410 In above tests we have assumed that the infill is made of the same material as the coating  
411 layer. The formulation (Eqs. 13 and 14) allows to use a different material representing the infill.  
412 Figure 16 shows an optimized cantilever beam using two different materials. The infill density  
413 field is grey, representing a relative density of  $\lambda_m = 0.6$ . A relative stiffness of  $\lambda_E = 0.6$  is tested  
414 for the infill material. Note that when using two different materials, the relative stiffness is not  
415 restricted to the Hashin-Shtrikman bounds as in the standard coating approach, which interprets  
416 the infill as a structural pattern made of the coating material. In this example it can be observed  
417 that in the opening at the left hand side the shell is not well formed around the left corner. This  
418 is a side effect of the introduced length scale control, as discussed in Section 4.3. Further studies  
419 and modifications may alleviate the issue, but since it only appears sporadically we leave this  
420 issue for future studies.

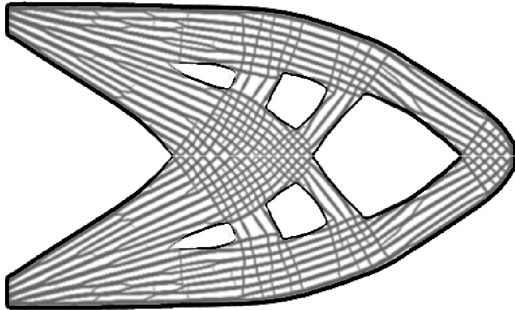


Figure 16: The shell-infill composite with a stiff material (black) for the shell, and a softer material (grey) for the infill.

## 421 6. Conclusion

422 We have presented a topology optimization method for evolving the shell and non-uniform  
 423 infill concurrently. The composite maintains a prescribed shell thickness, and its interior is filled  
 424 with non-uniform sparse structures up to a prescribed local volume fraction. The effectiveness  
 425 of the proposed shell-infill interpolation model has been confirmed through numerical tests.

426 Our results demonstrate that optimized, non-uniform infill performs better than uniform in-  
 427 fill for the same material volume. The optimized shell-infill shows some interesting geometric  
 428 patterns. Elongated infill is found in the uni-axially loaded bars, while crossing infill can be  
 429 observed at the joints connecting these bars. These results conform to, and can be explained by  
 430 our understanding of optimal structures. With the increasing fabrication flexibility offered by  
 431 additive manufacturing, it is expected that such tailor made structures will find many industrial  
 432 applications.

433 Extending the shell-infill formulation from 2D to 3D is straightforward. The 3D results for  
 434 the coating and the porous infill have been reported in [11] and [8], respectively. Closed-walled  
 435 (infill) structures are efficient for stiffness. However, they might trap unsintered powders in  
 436 powder-based fabrication. To steer closed-walled structures into truss-like structures, a possi-  
 437 ble solution is to restrict the local volume bound such that the locally allowable volume is not  
 438 sufficient to create closed-walled structures [8].

439 Despite a rather complicated optimization model that includes four successive filter opera-  
 440 tions the algorithm is remarkably robust to parameter and geometric variations. Additional runs  
 441 for other volume fractions and e.g., the classical MBB beam are easily solved and result in similar  
 442 conclusions and are hence left out for space reasons.

## 443 Acknowledgement

444 The authors gratefully acknowledge the support from the H.C. Ørsted Postdoc Programme at  
 445 the Technical University of Denmark, which has received funding from the People Programme  
 446 (Marie Curie Actions) of the European Union's Seventh Framework Programme (FP7/2007-  
 447 2013) under REA grant agreement no. 609405 (COFUNDPostdocDTU), and the support from  
 448 the Villum foundation through the InnoTop VILLUM Investigator project.

449 **References**

- 450 [1] M. P. Bendsøe, N. Kikuchi, Generating optimal topologies in structural design using a homogenization method,  
 451 Computer methods in applied mechanics and engineering 71 (2) (1988) 197–224. doi:[10.1016/0045-7825\(88\)90086-2](https://doi.org/10.1016/0045-7825(88)90086-2).
- 453 [2] M. P. Bendsøe, O. Sigmund, Topology optimization: theory, methods, and applications, Springer-Verlag Berlin  
 454 Heidelberg, 2004.
- 455 [3] O. Sigmund, K. Maute, Topology optimization approaches, Struct. Multidiscip. Optim. 48 (6) (2013) 1031–1055.  
 456 doi:[10.1007/s00158-013-0978-6](https://doi.org/10.1007/s00158-013-0978-6).
- 457 [4] J. D. Deaton, R. V. Grandhi, A survey of structural and multidisciplinary continuum topology optimization: post  
 458 2000, Struct. Multidiscip. Optim. 49 (1) (2014) 1–38. doi:[10.1007/s00158-013-0956-z](https://doi.org/10.1007/s00158-013-0956-z).
- 459 [5] I. Gibson, D. W. Rosen, B. Stucker, Design for Additive Manufacturing, Springer US, Boston, MA, 2010, pp.  
 460 299–332. doi:[10.1007/978-1-4419-1120-9\\_11](https://doi.org/10.1007/978-1-4419-1120-9_11).
- 461 [6] W. Gao, Y. Zhang, D. Ramanujan, K. Ramani, Y. Chen, C. B. Williams, C. C. Wang, Y. C. Shin, S. Zhang, P. D.  
 462 Zavattieri, The status, challenges, and future of additive manufacturing in engineering, Computer-Aided Design 69  
 463 (2015) 65–89. doi:[10.1016/j.cad.2015.04.001](https://doi.org/10.1016/j.cad.2015.04.001).
- 464 [7] A. Clausen, N. Aage, O. Sigmund, Exploiting additive manufacturing infill in topology optimization for improved  
 465 buckling load, Engineering 2 (2) (2016) 250 – 257. doi:[10.1016/J.ENG.2016.02.006](https://doi.org/10.1016/J.ENG.2016.02.006).
- 466 [8] J. Wu, N. Aage, R. Westermann, O. Sigmund, Infill optimization for additive manufacturing – approaching bone-  
 467 like porous structures, IEEE Transactions on Visualization and Computer Graphics PP (99) (2017) 1–1. doi:  
 468 [10.1109/TVCG.2017.2655523](https://doi.org/10.1109/TVCG.2017.2655523).
- 469 [9] M. P. Bendsøe, O. Sigmund, Material interpolation schemes in topology optimization, Archive of Applied Mechanics 69 (9–10) (1999) 635–654. doi:[10.1007/s004190050248](https://doi.org/10.1007/s004190050248).
- 470 [10] A. Clausen, N. Aage, O. Sigmund, Topology optimization of coated structures and material interface problems,  
 471 Computer Methods in Applied Mechanics and Engineering 290 (2015) 524 – 541. doi:[10.1016/j.cma.2015.02.011](https://doi.org/10.1016/j.cma.2015.02.011).
- 472 [11] A. Clausen, E. Andreassen, O. Sigmund, Topology optimization of 3d shell structures with porous infill, Acta  
 473 Mechanica Sinica (0) 1.
- 474 [12] J. Guest, Imposing maximum length scale in topology optimization, Struct. Multidiscip. Optim. 37 (5) (2009)  
 475 463–473. doi:[10.1007/s00158-008-0250-7](https://doi.org/10.1007/s00158-008-0250-7).
- 476 [13] B. S. Lazarov, F. Wang, Maximum length scale in density based topology optimization, Computer Methods in  
 477 Applied Mechanics and Engineering 318 (2017) 826 – 844. doi:[10.1016/j.cma.2017.02.018](https://doi.org/10.1016/j.cma.2017.02.018).
- 478 [14] F. Wang, B. S. Lazarov, O. Sigmund, On projection methods, convergence and robust formulations in topol-  
 479 ogy optimization, Structural and Multidisciplinary Optimization 43 (6) (2010) 767–784. doi:[10.1007/s00158-010-0602-y](https://doi.org/10.1007/s00158-010-0602-y).
- 480 [15] M. Langelaar, An additive manufacturing filter for topology optimization of print-ready designs, Struct. Multidis-  
 481 cip. Optim. (2016) 1–13doi:[10.1007/s00158-016-1522-2](https://doi.org/10.1007/s00158-016-1522-2).
- 482 [16] X. Qian, Undercut and overhang angle control in topology optimization: a density gradient based integral approach,  
 483 Int J Numer Meth Eng n/a–n/aNme.5461. doi:[10.1002/nme.5461](https://doi.org/10.1002/nme.5461).
- 484 [17] A. T. Gaynor, J. K. Guest, Topology optimization considering overhang constraints: Eliminating sacrificial support  
 485 material in additive manufacturing through design, Struct. Multidiscip. Optim. 54 (5) (2016) 1157–1172. doi:  
 486 [10.1007/s00158-016-1551-x](https://doi.org/10.1007/s00158-016-1551-x).
- 487 [18] J. K. Guest, J. Prévost, T. Belytschko, Achieving minimum length scale in topology optimization using nodal design  
 488 variables and projection functions, International Journal for Numerical Methods in Engineering 61 (2) (2004) 238–  
 489 254. doi:[10.1002/nme.1064](https://doi.org/10.1002/nme.1064).
- 490 [19] O. Sigmund, Morphology-based black and white filters for topology optimization, Structural and Multidisciplinary  
 491 Optimization 33 (4) (2007) 401–424. doi:[10.1007/s00158-006-0087-x](https://doi.org/10.1007/s00158-006-0087-x).
- 492 [20] S. Xu, Y. Cai, G. Cheng, Volume preserving nonlinear density filter based on heaviside functions, Structural and  
 493 Multidisciplinary Optimization 41 (4) (2010) 495–505. doi:[10.1007/s00158-009-0452-7](https://doi.org/10.1007/s00158-009-0452-7).
- 494 [21] J. Wu, C. C. Wang, X. Zhang, R. Westermann, Self-supporting rhombic infill structures for additive manufacturing,  
 495 Computer-Aided Design 80 (2016) 32 – 42. doi:[10.1016/j.cad.2016.07.006](https://doi.org/10.1016/j.cad.2016.07.006).
- 496 [22] B. S. Lazarov, F. Wang, O. Sigmund, Length scale and manufacturability in density-based topology optimization,  
 497 Archive of Applied Mechanics 86 (1) (2016) 189–218. doi:[10.1007/s00419-015-1106-4](https://doi.org/10.1007/s00419-015-1106-4).
- 498 [23] O. Sigmund, Design of multiphysics actuators using topology optimization part ii: Two-material structures,  
 499 Computer Methods in Applied Mechanics and Engineering 190 (4950) (2001) 6605 – 6627. doi:[10.1016/S0045-7825\(01\)00252-3](https://doi.org/10.1016/S0045-7825(01)00252-3).
- 500 [24] A. Díaz, O. Sigmund, Checkerboard patterns in layout optimization, Structural optimization 10 (1) (1995) 40–45.  
 501 doi:[10.1007/BF01743693](https://doi.org/10.1007/BF01743693).

- 506 [25] B. S. Lazarov, O. Sigmund, Filters in topology optimization based on helmholtz-type differential equations, International Journal for Numerical Methods in Engineering 86 (6) (2011) 765–781. doi:[10.1002/nme.3072](https://doi.org/10.1002/nme.3072).
- 507 [26] K. Svanberg, The method of moving asymptotes—a new method for structural optimization, International Journal for Numerical Methods in Engineering 24 (2) (1987) 359–373. doi:[10.1002/nme.1620240207](https://doi.org/10.1002/nme.1620240207).
- 508 [27] O. Sigmund, Manufacturing tolerant topology optimization, Acta Mechanica Sinica 25 (2) (2009) 227–239. doi:[10.1007/s10409-009-0240-z](https://doi.org/10.1007/s10409-009-0240-z).
- 509 [28] A. Clausen, E. Andreassen, On filter boundary conditions in topology optimization, Structural and Multidisciplinary Optimization doi:[10.1007/s00158-017-1709-1](https://doi.org/10.1007/s00158-017-1709-1).
- 510 [29] Z. Hashin, S. Shtrikman, A variational approach to the theory of the elastic behaviour of multiphase materials, Journal of the Mechanics and Physics of Solids 11 (2) (1963) 127 – 140. doi:[10.1016/0022-5096\(63\)90060-7](https://doi.org/10.1016/0022-5096(63)90060-7).
- 511
- 512
- 513
- 514
- 515